

Thermal Features of Lunar Regolith in Mare Humboldtianum based on Brightness Temperature Differences and Surface Parameters

Wei Cao¹, Zhiguo Meng², Aiju Li³, Jietao Lei², Xuegang Dong², Ting Lan⁴, Jiannan Zhao⁵, Zhanchuan Cai⁶, and Binghua Su⁷

¹Beijing Institute of Technology, Zhuhai, China

²Jilin University

³Shandong transport vocational college, China

⁴Macau University of Science and Technology

⁵University of Geosciences

⁶Macau university of science and technology

⁷Beijing Institute of Technology

November 24, 2022

Abstract

Mare Humboldtianum is a Nectarian-aged basin on the northeast limb of the Moon, whose inner ring was flooded by basalt billions of years ago. The topography of Mare Humboldt is rather complex, which makes it difficult to define the basaltic units only by the spectral data. To improve understanding of the geological units in Mare Humboldt and provide new interpretations of the formation process, we use the brightness temperature (TB) data obtained by the Chang'E-2 (CE-2) mission, which is proved to have a good penetration feature. The TB difference (dT_B) maps at multichannels are created to analyze the TB variations. The Backpropagation Neural Network (BPNN) model is first used to provide a statistical interpretation of the relation between dT_B distributions and surface parameters. Our results show that, most of the dT_B performances are strongly affected by the topography. Several abnormally dT_B performances are observed on dT_B maps. This observation indicates that there exists two different mare units in the eastern and western parts in the basin floor. These TB variations are interpreted that most of the dT_B anomalies are strongly related to the special tectonic features. The statistical results based on BPNN method indicate that multichannel TB variations reflect different topographic features. Most of the topographic effects related to dT_B variations are found in the regions controlled by the small craters and topographic bulges in the basin floor.

Abstract

Mare Humboldtianum is a Nectarian-aged basin on the northeast limb of the Moon, whose inner ring was flooded by basalt billions of years ago. The topography of Mare Humboldtianum is rather complex, which makes it difficult to define the basaltic units only by the spectral data. To improve understanding of the geological units in Mare Humboldtianum and provide new interpretations of the formation process, we use the brightness temperature (TB) data obtained by the Chang'E-2 (CE-2) mission, which is proved to have a good penetration feature. The TB difference (dT_B) maps at multichannels are created to analyze the TB variations. The Backpropagation Neural Network (BPNN) model is first used to provide a statistical interpretation of the relation between dT_B distributions and surface parameters. Our results show that, most of the dT_B performances are strongly affected by the topography. Several abnormally dT_B performances are observed on dT_B maps. This observation indicates that there exists two different mare units in the eastern and western parts in the basin floor. These TB variations are interpreted that most of the dT_B anomalies are strongly related to the special tectonic features. The statistical results based on BPNN method indicate that multichannel TB variations reflect different topographic features. Most of the topographic effects related to dT_B variations are found in the regions controlled by the small craters and topographic bulges in the basin floor.

Plain Language Summary

The brightness temperature (TB) data collected by Chang'E-2 spacecraft provides an opportunity to study the thermal and dielectric properties of lunar regolith. Mare Humboldtianum exposes typical basalt materials, which can reflect the thermophysical features of the basin. In this paper, we evaluated the thermophysical features of Mare Humboldtianum based on the TB difference (dT_B) maps at multichannels. The surface parameters are calculated to interpret the dT_B distributions. We find that the dT_B anomalies in the study region show strong correlation with the tectonic features. Compared with the surface parameters, dT_B distributions reflect different topographic features at different frequencies.

1 Introduction

Mare Humboldtianum (Figure 1) is an Imbrian-age multiring basin located within Humboldtianum basin with a 650 km wide (Hiesinger et al., 1996). Typical ring terraces can be observed clearly in the digital terrain model with a grid spacing of 2 km and a height resolution of 500 m (Oberst et al., 1996). The inner ring of Mare Humboldtianum exposed extensive dark mare basalts (Moriarty & Pieters, 2016). Several smooth basalt exposures are presented in the area between the inner and outer basin rings. Both the central Mare Humboldtianum basalts and the inter-ring basalts exhibit a range in composition and age (Hiesinger et al., 1996, 2000). A basaltic composition is rich in high-Ca pyroxene based on the M3 target data with high spectral resolutions (Moriarty & Pieters, 2016). The basaltic volcanism of the basin center lasted longer than in the inter-ring area. The gravitational data from the Lunar Prospector spacecraft shows that Humboldtianum harbours a mass concentration (mascon) — a localized gravitational anomaly that tugs on orbiting spacecraft and suggests that the mascon is due to the presence of dense lunar mantle material lying within about 15 km of the surface (Booker et al., 1970; Freed et al., 2014).

The definition of homogeneous basaltic units is an important task to understand the nature and evolution of lunar basaltic volcanism (Hiesinger & Head, 2003; Hiesinger et al., 2010). For the geological unit definitions in Mare Humboldtianum, Hiesinger et al. (2000, 2011) provided the basaltic volcanism based on spectral data. The mare basalts in Mare Humboldtianum were therefore divided into 11 basalt units, where four units

were in the basin floor, called HU6, HU9, HU10, and HU11 (Figure 1). Moreover, Fortezzo et al. (2020) considered that two main geological units existed in the inner basalt area: Imbrian Upper Mare Units (Im2) and Imbrian/Nectarian Terra units (INt). Im2 was caused by the basaltic lava flows and INt was the rolling terrain with complex formations by the erosional debris and basin ejecta. Other units, such as Lower Imbrian Mare Units (Im1) and Lower Imbrian Crater units (Ic1), also consisted of the topographies of the typical terrains and areas. Although the previous literatures provided significant definitions of basaltic units in Mare Humboldtianum, the crater deposits, wrinkle ridges, and mare basalts in the floor also affected the spatial distributions of geological units. To improve the understanding of the basalt units in the basin floor, Meng et al. (2018, 2019, 2020) showed that the Chang'E-2 microwave radiometer (CELMS) data could provide a way to improve the understanding of the definition of the mare geological units and the formation process of lunar basins.

Passive microwave remote sensing has been used to study the variations of lunar regolith properties (Zheng et al., 2012; Feng et al., 2020). The CELMS instrument worked at frequencies of 3, 7.8, 19.35 and 37GHz to obtain numerous data of lunar brightness temperature (TB) at 24 hours (Table. 1). These TB data are determined by the received solar energy and the thermal properties of the lunar regolith (Zheng et al., 2019). The 2C-level CELMS data with calibration are widely used in thermophysical feature analysis of Moon (Fang & Fa, 2014; Hu et al., 2015, 2018; Zhu et al., 2019). The latitude tendencies of the TB variations are obvious, which affect the evaluation of the basaltic units in the basin (Meng et al., 2020). Therefore, we create the TB difference (dT_B) maps at 3, 7.8, 19.35, and 37GHz to improve the understanding of the thermophysical features of Mare Humboldtianum. dT_B is defined as the TB differences between the TB data collected at noon and in the early morning (Meng et al., 2018, 2019, 2020).

Since the antenna footprints of CELMS data are 17.5 km (7.8, 19.35, and 37GHz) and 25 km (3GHz), the thermophysical features of the geological units smaller than the 17 km scale are difficult to understand. Therefore, some surface parameters are used to interpret the dT_B variations at multichannels. Surface parameters are calculated for analyzing the geometrical properties of the surface (Olaya, 2009). In planetary surface analysis, surface parametrizations have been developed for a long time (Shepard et al., 2001; Kreslavsky & Head, 2000; Rosenburg et al., 2011; Kreslavsky et al., 2013; Cao et al., 2015; B. Li and X. Wang and J. Zhang and J. Chen and Z. Ling, 2016; Fa et al., 2016; Cao & Cai, 2018; Susorney et al., 2017, 2018, 2019; Cai & Fa, 2020). In this study, topographic roughness (Cao et al., 2018), Digital Terrain Entropy (DTE) (Lan et al., 2020), Slope, Aspectm, plane curvature (kh), and curvature (kv) (Li et al., 2017) are used for the correlation analysis of dT_B variations. These parameters are calculated based on the SL-DEM (Barker et al., 2016) and Lunar Orbit Laser Altimeter (LOLA) Gridded Data Records (GDRs) (Smith et al., 2010), which can be downloaded in <http://imbrium.mit.edu/>. Topographic roughness can provide 1 km-scale roughness textures for terrain analysis based on SLDEM. Other parameters can reflect 1.8 km-scale surface variations based on LOLA GDRs.

The paper is organized as follows. Section. 2 introduces the data processing and the details of the analyzed method. Section 3 provides a overview of the dT_B maps of Mare Humboldtianum. Section 4 discusses the cause of the typical TB variations and analyzes the statistical correlations between dT_B distributions and the surface parameters. The conclusion is stated in Section 5.

2 CELMS Data Processing and Surface Parameterizations

Since the latitude tendencies of TB data (Meng et al., 2018, 2019, 2020), dT_B maps are created to reduce this effect in thermal feature analysis of Mare Humboldtianum. Moreover, high-resolution Digital Elevation Models (DEMs) of lunar topography can provide

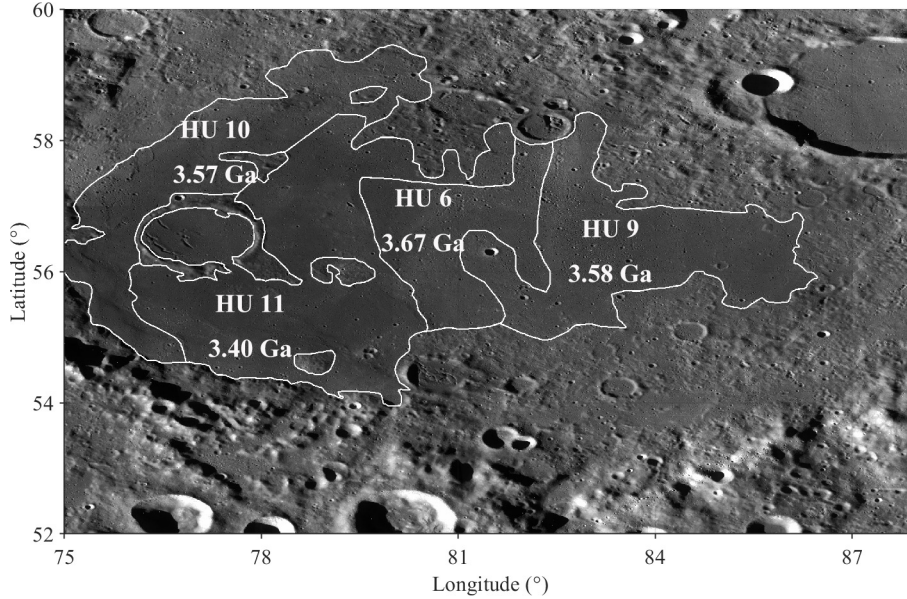


Figure 1: Basaltic units of Mare Humboldtianum. The geological boundaries are created based on the results in Hiesinger and Head (2003). The model ages of these geological regions were estimated by Hiesinger et al. (2011) (Unit: Ga). The base map is the LRO WAC image, which is derived from the Quickmap (<https://quickmap.lroc.asu.edu/>).

125 abundant topographic information for the identification and characterization of craters,
 126 basins and important data for understanding the impact process and history, thermal
 127 evolution, large events of lunar surface (Head et al., 2010; Baker et al., 2012; Fassett et
 128 al., 2012). Therefore, some surface parameters are used for thermophysical feature anal-
 129 ysis indicated by dTB distributions based on the lunar high-resolution DEMs. Topographic
 130 roughness shows the 1 km-scale textural map to interpret the dTB distributions. Other
 131 surface parameters are used for correlation analysis with multichannel dTB values.

132 2.1 TB Difference (dTB) Maps

133 The CELMS data are collected by the microwave radiometer onboard the Chang'E-
 134 2 (CE-2) spacecrafts. The antenna footprint of CE-2 MRM is 17.5 km for 7.8, 19.35, and
 135 37 GHz channels, and 25 km for 3GHz (Lan & Cai, 2018). The CELMS data in 2C level
 136 are collected by CE-2 satellite from October 2010 to June 2011. The 2C-level CELMS
 137 data are the raw TB data with geometric correction and radiometric calibration (Fang
 138 & Fa, 2014; Hu et al., 2018). These data are widely used for studying microwave ther-
 139 mal emission features (Lan & Cai, 2018; Zhu et al., 2019; Meng et al., 2020). In this study,
 140 we use the 2C-level CELMS data as the source data.

141 To reduce the effect of TB latitude tendencies, we create the dTB maps at 3, 7.8,
 142 19.35, and 37GHz. Based on the comparison of the TB distributions at every hour (Fig-
 143 ure 2), the TB data at 11 and 13 o'clock for noon, and 2 and 4 o'clock for early morn-
 144 ing are better to generate the dTB maps. Since the number of TB data is not enough
 145 to cover the whole area of Mare Humboldtianum, the raw data are gridded by the lin-
 146 ear interpolation (Meng et al., 2018, 2019).

147 The TB differences (dTB) between noon TB and night TB at the same frequen-
 148 cies is directly related to the regolith thermophysical parameters within the penetration
 149 depth of the corresponding microwave data (Meng et al., 2019, 2020). Since the TB points

Table 1: The number of global TB data at one day (24 hours)

Hour	The Number of TB Points ^a
0	321724
1	520454
2	514494
3	363131
4	327261
5	337407
6	337400
7	333915
8	315842
9	304989
10	282362
11	272508
12	319624
13	521174
14	520532
15	368434
16	338646
17	345198
18	344377
19	333046
20	318199
21	309892
22	287008
23	272867

^a the numbers of TB data with different frequencies at one hour are the same.

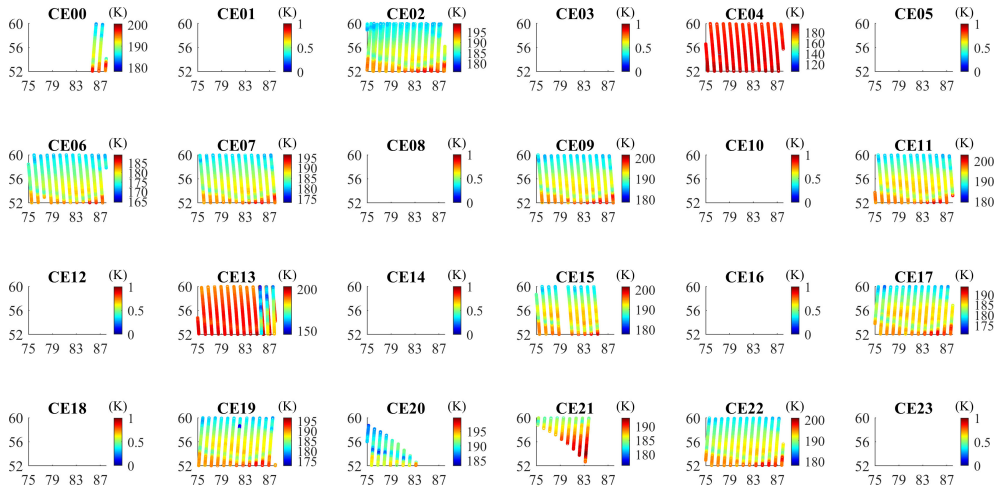


Figure 2: The raw TB data of Mare Humboldtianum at 24 hours, where x -axis and y -axis denote the longitudes and latitudes, respectively. The titles CE01-23 denote the hours. The data at 2, 4, 11 and 13 o'clock provide better qualities and enough points for TB map generation.

150 are scattered in the latitude-longitude coordinate system, the scattered TB points are
 151 interpolated by the triangulation-based linear interpolation. All the interpolated points

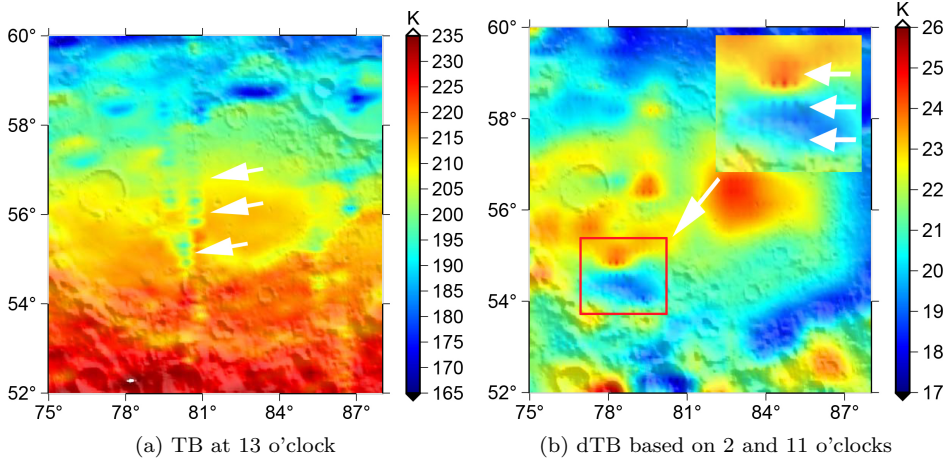


Figure 3: The TB and dTB abnormal values: (a) The abnormal TB values along latitudes; (b) dTB abnormal values based on the TB data at 2 and 11 o'clocks. White arrows point to these abnormal values on the maps. Red circle denotes the abnormal dTB values on the maps.

152 are located inside the convex hull of the original data points. Some interpolated points
 153 at the edges are defined as NaN values. To solve this problem, the interpolated latitudes
 154 and longitude values (La and Lo) are expressed as follows:

$$155 \quad La = [\max(la) - \min(la) + 4] * a \quad (1)$$

$$156 \quad Lo = [\max(lo) - \min(lo) + 4] * a \quad (2)$$

158 where la and lo denote the original latitude and longitude value, respectively. The value
 159 4 means that additional four original points are used in the interpolation to remove the
 160 effect of NaN values. The redundant interpolated points at the edges are deleted after
 161 the interpolation. a denotes the interpolated points for one degree. Therefore, the in-
 162 terpolated TB values can be expressed as follows:

$$163 \quad TB_{time} = linear(La, Lo, (la, lo, rTB)) \quad (3)$$

164 where $time$ denotes the local hour in Table 1. The function *linear* denotes the linear *grid-*
 165 *date* function in MATLAB software. The linear function are fitted by the raw data (la, lo, rTB) ,
 166 where rTB denotes the TB values of CE-2 2C-Level data.

167 The interpolated TB maps have resolutions of $0.25^\circ \times 0.25^\circ$. The dTB maps (3GHz,
 168 7.8GHz, 19.35GHz, and 37GHz) can be expressed as:

$$169 \quad dTB = TB_n - TB_m \quad (4)$$

170 where TB_n and TB_m denote the interpolated TB maps at noon and in the early morn-
 171 ing, respectively.

172 To provide the reasonable observations of dTB variations, we test the TB data at
 173 2, 4, 11, 13 o'clocks by creating their TB or dTB maps. At the channel 19.35GHz, we
 174 find some abnormal data in the TB data at 13 o'clock and dTB map based on TB data
 175 at 2 and 11 o'clocks. As shown in Figure 3, the abnormal TB data at 13 o'clock can be
 176 observed along the latitudes nearby $81^\circ E$ (Figure 3(a)). In Figure 3(b), the dTB maps
 177 based on the TB data at 2 and 11 o'clock show some abnormal TB data along the lat-
 178 itudes (large window with three white arrows). Therefore, we select the TB data at 4
 179 and 11 o'clock to create the multichannel dTB maps (Figure 4).

180

2.2 Surface Parameterizations

In this study, topographic roughness calculated in Cao et al. (2018) can quantify the amplitude of topographic features of elevations at a horizontal scale. The roughness values are expressed as:

$$R\left(\frac{M}{2}, \frac{M}{2}\right) = \frac{1}{M \times M} \left(\sum_{x=1}^n \sum_{y=1}^n M_{matrix}(x, y) Z(y, x) M_{matrix}^T(x, y) \right) \quad (5)$$

181

182

183

184

185

where M is the number of pixels in the moving window. M_{matrix} denotes the V-system matrix created by the V-system series (Song et al., 2007). R denotes the parametrized value of roughness centred at the scale (defined as a moving window with size of $M \times M$). Z is the DEM determined by the $M \times M$ moving window. x and y denote the latitude and longitude, respectively.

DTE (Lan et al., 2020) is a surface parameter used to reflect the quantity of the geomorphic information obtained in the DEMs:

$$DTE = - \sum \sum p \log_2 p \quad (6)$$

186

where p denotes the the ratio of the elevation value of a local point on lunar surface.

187

188

Other parameters are provided by Li et al. (2017). The calculations of these parameters are given as follows.

Slope is defined as the elevation variability of lunar topography, which can be expressed as follows:

$$Slope = \arctan \sqrt{F_x^2 + F_y^2} \times 180^\circ / \pi \quad (7)$$

189

190

where F_x^2 and F_y^2 denote the elevation change rates in the longitude and latitude, respectively.

Aspectm can determine the amount of solar radiation, which influences local site microclimate (Ahmadzadeh & Petrou, 2001). In this study, Aspectm is defined as the ratio of the given pixel at the longitude x and latitude y :

$$Aspectm = \arctan(F_y^2 / F_x^2) \quad (8)$$

191

where F_x^2 and F_y^2 are the same as those in Equation. 7.

Curvature provides a quantitative measurement to quantify the pixels' distortion degree of DEMs. In this study, the curvatures calculated by the pixels at horizontal and vertical directions are called plane curvature (k_h) and section curvature (k_v), respectively. The expressions of these parameters are given as follows:

$$k_v = - \frac{p^2 r + 2pqs + q^2 t}{(p^2 + q^2) \sqrt{1 + p^2 + q^2}} \quad (9)$$

$$k_h = - \frac{q^2 r + 2pqs + p^2 t}{(p^2 + q^2) \sqrt{1 + p^2 + q^2}} \quad (10)$$

where p , q , r , s , and t can be expressed based on the local DEM z (Li et al., 2017):

$$p = \frac{\partial z}{\partial x}, q = \frac{\partial z}{\partial y}, r = \frac{\partial^2 z}{\partial^2 x}, s = \frac{\partial^2 z}{\partial x \partial y}, t = \frac{\partial^2 z}{\partial^2 y} \quad (11)$$

192

where x and y denote the longitude and latitude, respectively.

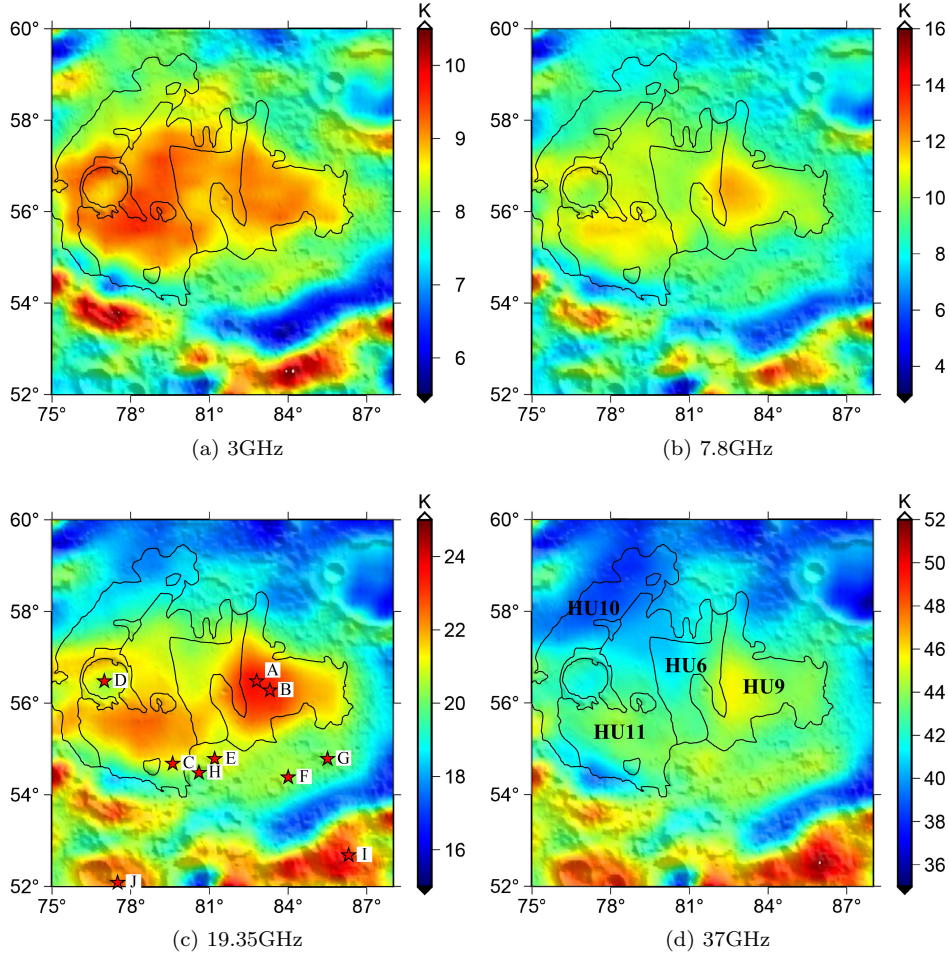


Figure 4: Multichannel dTB gridded maps created based on the TB data at 4 and 11 o'clock. Black lines denote the geological boundary marked in Figure 1. The points in (c) show typical dTB performances, where A: (82.8°E, 56.5°N); B: (83.3°E, 56.3°N); C: (79.6°E, 54.7°N); D: (77°E, 56.5°N); E: (81.2°E, 54.8°N); F: (84°E, 54.4°N); G: (85.5°E, 54.8°N); H: (80.6°E, 54.5°N); I: (86.3°E, 52.7°N); J: (77.5°E, 52.1°N). The names of defined units are marked in (d).

3 Results

3.1 Multichannel dTB maps

Figure 4 shows the dTB maps at 3, 7.8, 19.35, and 37GHz. The related histograms of dTB values are given in Figure 5. The geological boundaries (Hiesinger & Head, 2003; Hiesinger et al., 2011) are marked in the figures. At 19.35GHz (Figure 4(c)), we mark some typical dTB variations on the maps for thermophysical feature analysis of mare deposits and the names of defined units are shown in Figure 4(d). As a systematic overview, the dTB values become larger following with the frequency increases. The dTB performances in the western part of the basin floor are complex. At 3.0 GHz, the dTB here is similar as that in the eastern part. But from 7.8 GHz, the dTB in the western part is clearly lower than that in the eastern part. Particularly, at 37 GHz, the dTB is similar to the extensive regions in the Basin floor, which is about 2 K lower than that in the

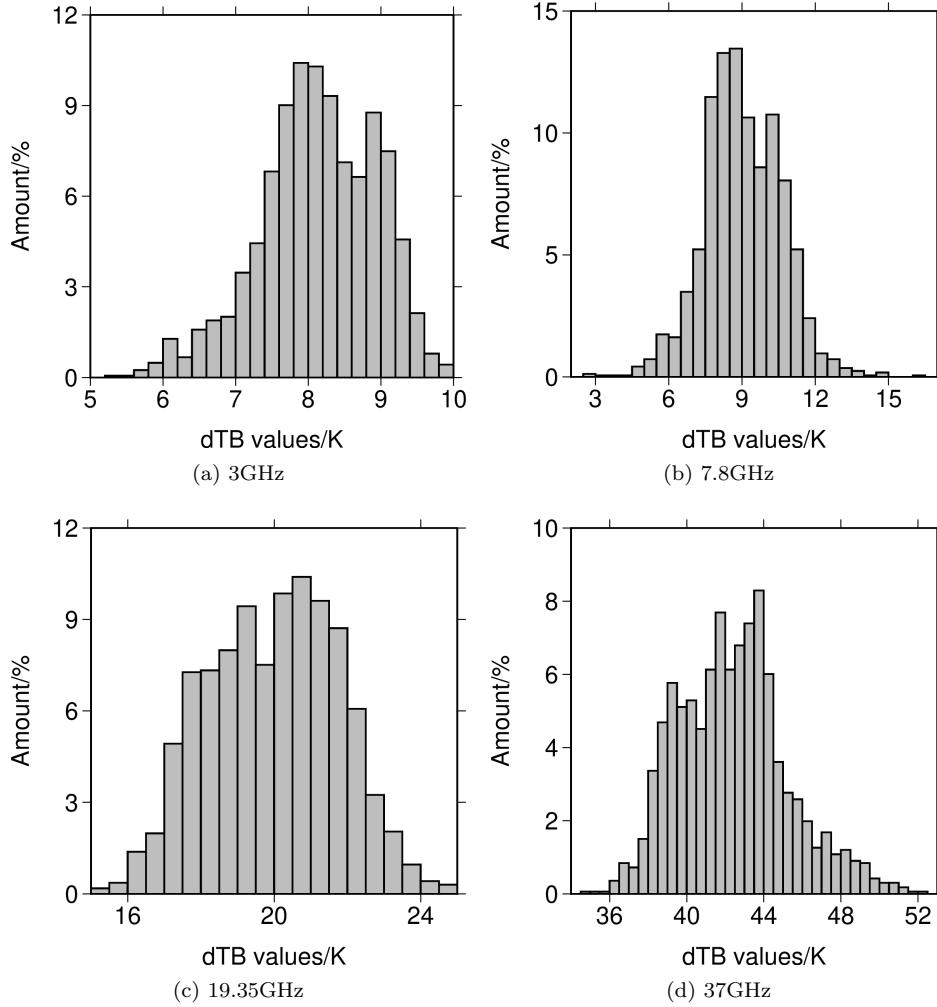


Figure 5: The histograms of dTB values at (a) 3GHz; (b) 7.8GHz; (c) 19.35GHz; (d)37GHz.

205 eastern part. More details of the dTB distributions at each channel are provided as fol-
 206 lows:

207 At 3GHz (Figure 4(a)), dTB values varies from 5.4 to 10.9 K. The interval of his-
 208 togram bin boundaries is 0.2 (Figure 5(a)). Three clusters of high dTB distributions (\geq
 209 10) can be observed in HU6, HU9, HU10, and HU11. The cluster with highest values
 210 is clearly related to the regions covered by the mare basalts, while the area is smaller
 211 than those indicated by the optical data. The clueset with lowest values is clearly related
 212 to the regions in the southern part of HU11, which is likely brought by the low volumet-
 213 ric temperature for the topography opposite to the solar illumination (Meng et al., 2019).
 214 And the rest regions are responsible for the cluster with middle values.

215 At 7.8GHz (Figure 4(b)), the dTB varies from 2.7 to 16.9 K. The interval of his-
 216 togram bin boundaries is 0.5 (Figure 5(b)). Most of the obvious high dTB values are
 217 appeared in the western part of HU9, and other parts can be seen in HU6. HU10 also shows
 218 high dTB distributions (≥ 12), which are in the south of the crater (centered at point
 219 D). Three clusters of high dTB distributions (≥ 10) can also be observed in HU6, HU9,
 220 HU10, and HU11. The cluster with highest values is much smaller than that at 3.0 GHz,

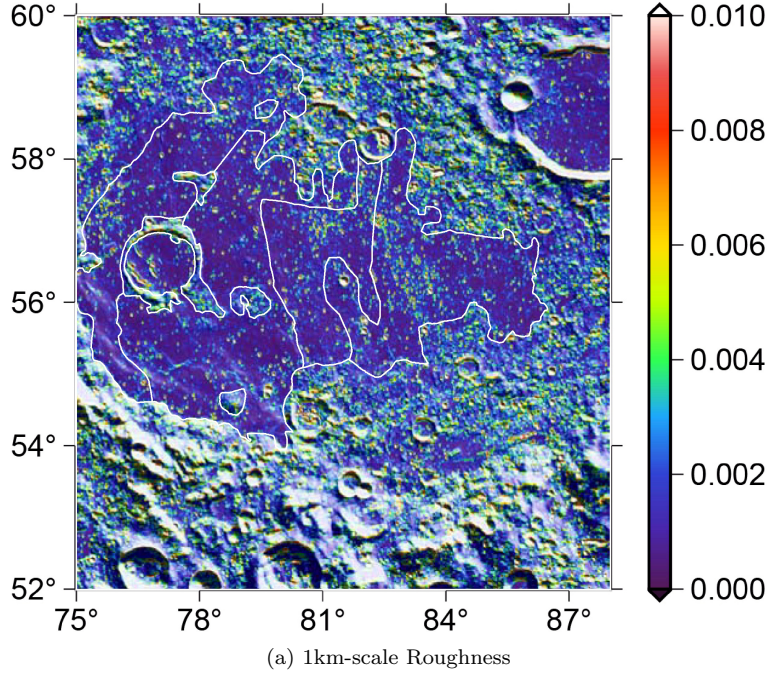


Figure 6: Topographic roughness map created by Cao et al. (2018). The white lines denote the geological boundaries marked in Figure 1.

221 which is related to two small patches centered at Point A and at the northwest place of
 222 Point C. The cluster with lowest values is clearly related to the regions in the northern
 223 part of HU10 and the southern part of HU11. And the rest regions are responsible for
 224 the cluster with middle values, which is extensively distributed in the Mare floor.

225 At 19.35GHz (Figure 4(c)), the interval of dTB differences become larger (from 15.1
 226 to 25.0 K). The interval of histogram bin boundaries is 0.5 (Figure 5(c)). Mass high dTB
 227 distributions (≥ 22) are local in HU9 and HU11. A cluster of dTB distributions (≥ 22),
 228 which is appeared in the southern part of HU6, “connects” the high dTB distributions
 229 in HU9 and HU11. Two dTB clusters can be observed in HU6, HU9, HU10, and HU11.
 230 The cluster with higher values is related to two small patches centered at Point A and
 231 at the northwest place of Point C. The cluster with lower values is clearly related to the
 232 regions in the northern parts of Hu6, 10 and 11.

233 At 37GHz (Figure 4(d)), the range of dTB changes is from 34.6 to 52.5 K. The in-
 234 terval of histogram bin boundaries is 0.5 (Figure 5(d)). Most of dTB variations (≥ 46)
 235 are local in the western part of HU9. Four clusters of high dTB distributions (≥ 44) can
 236 be observed in HU10, HU11, and HU9, HU6. The cluster with highest values is related
 237 to patch centered at Point A. The cluster with second highest values is related to the
 238 patch centered at the northwest place of Point C. The cluster with lowest values is clearly
 239 related to the regions in the northern part of Hu6, HU10, HU11 and the southern part
 240 of HU11. Such dTB performances at different frequency also hint a good description of
 241 the change of the regolith thermophysical features with depth.

242 In conclude, The dTB values in HU9 and HU11 show most of the high dTB dis-
 243 tributions at multichannels. These dTB distributions show different result from the unit
 244 definition in Hiesinger et al. (2011).

245

3.2 Topographic roughness map

246

247

248

249

250

251

252

253

254

255

256

The 1 km-scale topographic roughness (Cao et al., 2018) is mapped to analyze the topographic features related to typical dTB variations (Figure 6). As a systematic overview, topographic roughness cannot show obvious linear relationships to the dTB variations. High roughness textures (green to yellow colorshades, from 0.004 to 0.006 in Figure 6) caused by the small craters in HU9, the edges of the bulge in HU11, and the crater rims centered at point D. In HU9, high roughness variations can be seen the area centered at point A (Figure 4(a)-(d)) and caused by the small craters. The cluster of these craters indicates high roughness distributions with banded structures. Some high roughness textures distribute near the topographic bulges and in the small craters at the south parts of HU11. Other high roughness textures appear in the crater rims centered at point D. The low roughness values are caused by the smooth and young mare basalts (Figure 1).

257

258

259

260

261

262

263

264

265

266

267

268

269

As a systematic overview, the roughness textures in the units defined in Hiesinger et al. (2011) cannot show similar or homogeneous textural variations and distributions. Small craters, deposits on crater rims and topographic bulges cause the high roughness values. Compared with the dTB distributions (Figure 4), high dTB regions (HU9 and HU11) indicate different roughness features. In HU9, the scattered roughness textures are mainly caused by the northern small crater. The scattered textural variations are from northwestern to southern parts of HU9. These roughness variations are related to the high dTB variations in Figure 4(d), because dTB values decrease from western to eastern parts of HU9. In HU11, high dTB values can be observed near the crater rim (Figure 4). The roughness textures indicate two high linear distributions, which are caused by the small craters and topographic bulges (Figure 1), from southwestern to northeastern parts of HU11. High dTB distributions can be seen in the region between the two linear roughness textures, and are related to low roughness textures.

270

271

272

273

Thus, the roughness textures show a different unit distributions from the previous results (Hiesinger & Head, 2003; Hiesinger et al., 2011). Moreover, high roughness textures indicate that high dTB distributions are mainly related to the scattered topographic variations caused by small craters and topographic bulges.

274

4 Discussions

275

4.1 Re-evaluation of mare basalt units

276

277

278

279

In this part, we provide the analysis of dTB distributions to show that: (1) the visible data is not rational to reflect thermophysical features in the study area; (2) dTB performances can indicate new descriptions about basaltic units and related volcanic activities.

280

281

282

283

284

285

286

287

288

289

290

291

292

293

294

Hiesinger et al. (2011) subdivided the western part into HU10 unit aged 3.57 Ga in the western part and HU11 unit aged 3.40 Ga in the eastern part. However, the difference between the two units is not clearly in the dTB maps. Therefore, the geologic units identified only with visible data should be severely treated. Moreover, Figure 7 shows that the FTCs in the southern part are higher than those in the northern part. Correspondingly, the dTB in the former is apparently higher than that in the latter, validating the strong correlation between the FTCs and the dTB values. Figure 4 indicates that there exists a bad correspondence between the dTB performances and the basaltic units (Hiesinger & Head, 2003; Hiesinger et al., 2011). Figure 8 indicates the histograms of dTB values in the defined basaltic units. Theoretically, each peak in the histogram denotes one type of basalt units. HU6 can show four types of basaltic units at multichannels (Figure 8(a)). However, there are only three types of basalt units shown in HU9 (Figure 8(b)), HU10 (Figure 8(c)), and HU11 (Figure 8(d)), which are clearly related to the dTB in the basin floor (relatively higher values), the region surrounding the basin floor, and the nearby highlands (relatively lower values) as mentioned in Section 3. That is,

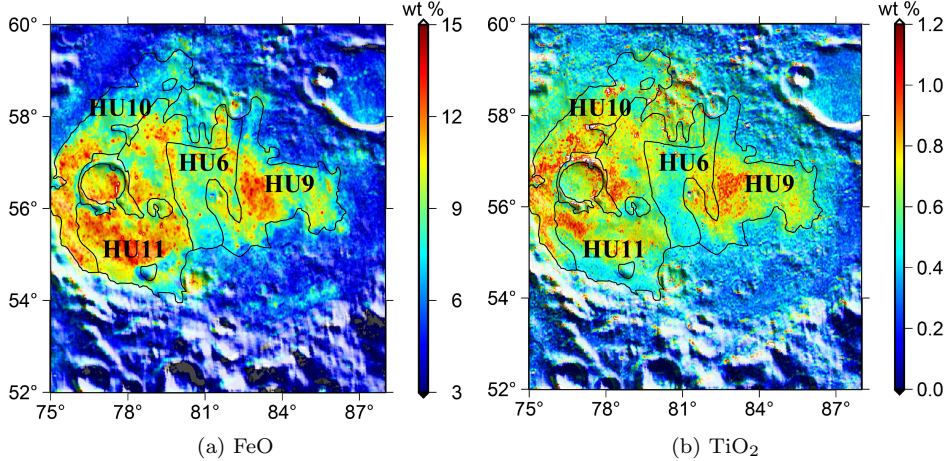


Figure 7: FeO and TiO₂ contents (FTCs) used for TB analysis. (a) FeO; (b) TiO₂. The black lines denote the geological boundaries marked in Figure 1.

295 the previous division of the basalt units only by visible data is not rational to reflect the
 296 thermophysical features of the mare units.

297 According to the previous studies of the mare basalts with CELMS data (Meng et
 298 al., 2018, 2019, 2020), the high dTB is probably related to the high FeO+TiO₂ contents
 299 (FTCs) of the mare deposits. Therefore, the FTCs estimated with the Clementine UV-
 300 VIS data using the Lucey method are employed in this study (Figure 7). Figure 4
 301 postulates that the dTB can mainly be divided into three categories. The first category is
 302 the basin center with the highest dTB. The dTB performances in this category are ap-
 303 parently dominated by the FTCs (Figure 7(a) and (b)). The second category is the north-
 304 ern part of units HU6 and HU10, where the dTB and the FTCs are clearly lower than
 305 the remanet part of the mare places. The third category is the the northern and south-
 306 ern rims of the Humboldtianum, which indicates the second lowest and highest dTB val-
 307 ues, respectively. Considering the deficient solar illumination in the northern part and
 308 the enhanced solar illumination in the southern part of the Basin wall, the dTB perfor-
 309 mances here are highly related to the topography opposite to the solar illumination. That
 310 is, the dTB performances in the study area should be strongly affected by the topogra-
 311 phy. Interestingly, we mentioned that the relatively larger craters in the basin floor, the
 312 dTB is similar surrounding the craters wall, indicating that the influence of the topog-
 313 raphy on the dTB is limited. Moreover, the dTB performances show a fairly strong cor-
 314 relation with the FTCs (Figure 7(a) and (b)), indicating that the FTC is the dominated
 315 factor of the dTB. Thus, the dTB maps imply a good description of the basaltic units
 316 in the study area.

317 Generally, the dTB performances indicate a new description about the basaltic vol-
 318 canism in Mare Humboldtianum. At first, the geologic boundaries interpreted by Hiesinger
 319 et al. (2011) are not identified by the dTB performances. But according to the dTB per-
 320 formances, the mare basalts can be subdivided into the eastern and western parts in the
 321 Basin floor. The difference between the optical result and the microwave result is likely
 322 brought by the strong contamination of the ejecta from the faraway places. Secondly,
 323 in this small time range, the youngest basalt should be in the eastern part of the Basin
 324 floor, where the highest dTB values imply that the FTCs should be much higher than
 325 those in the western part. Especially, we mentioned that the apparent distribution of the
 326 ejecta in the eastern unit. Moreover, the craters distributed in boundary lines also in-
 327 dicate the strong influence of the ejecta from the faraway places. That is, the eastern

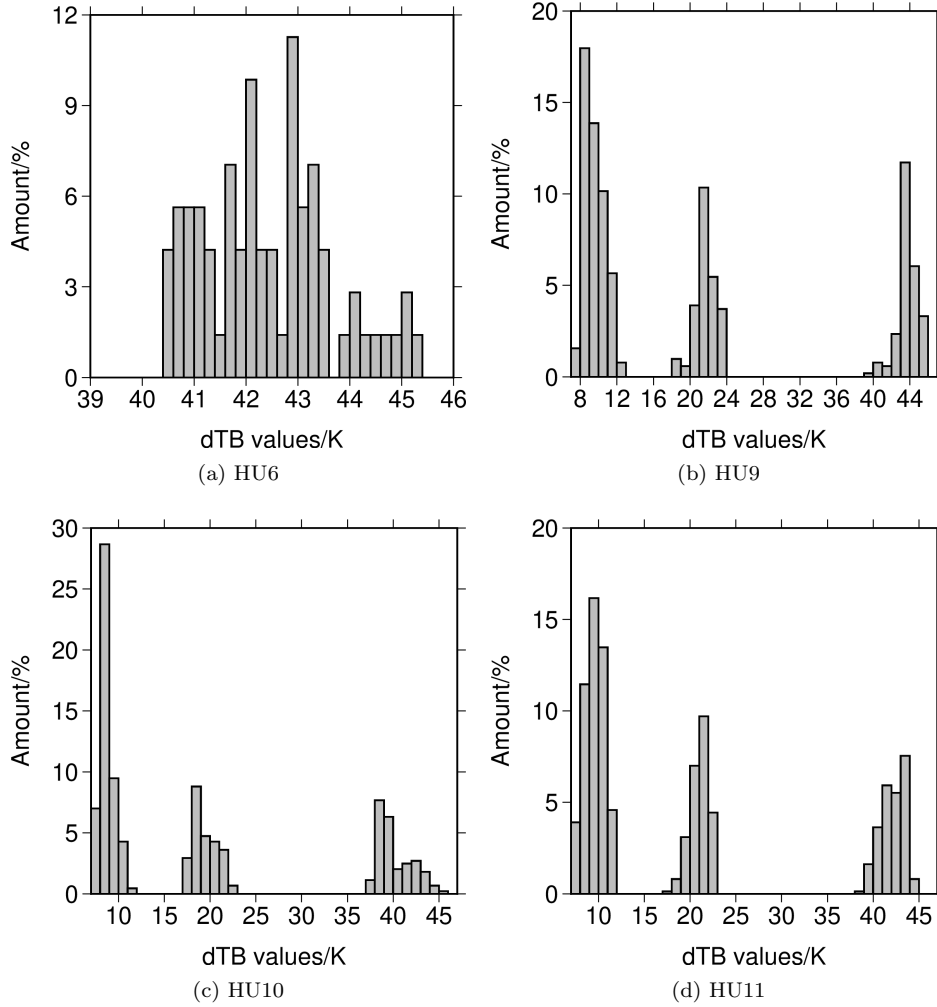


Figure 8: The histograms of dTB values of the defined geological units (HU6, HU9, HU10, and HU11) in Mare Humboldtianum (Hiesinger et al., 2011) at multichannels (3, 7.8, 19.35, and 37GHz). Each histogram contains all the dTB values of the defined geological units at the selected channels.

328 region with high dTB anomaly should be strongly altered by the impact ejecta in the
 329 surface layer, which decreased the surface FTCs and elevated the calculated surface age.
 330 Thus, what we found about the basaltic volcanism should be rational according to the
 331 microwave radiometer data with considerable penetration ability.

332 4.2 dTB Anomaly

333 Figure 4(c) indicates that there exists an abnormally high dTB zone centered at point
 334 A (82.8°E, 56.5°N) in the eastern part of the Basin floor. Here, high dTB anomaly is
 335 about 85 km × 55 km at 3.0 GHz, which is about 2 K evenly higher than its east vicin-
 336 ity. The anomaly keeps constant at 7.8 and 19.35 GHz, while there occurs a small patch
 337 with highest dTB centered at point A (82.8°E, 56.5°N) with a 15-km diameter at 7.8
 338 GHz and it extends to the 30-km diameter at 19.35 GHz. At 37 GHz, the high dTB anomaly
 339 decreases to a smaller patch centered at point A (82.8E, 56.5N) with the size of 35 km
 340 × 45 km, which is also about 2 K higher than its vicinity.

341 What brought the high dTB anomaly? No wrinkle range or apparent cones are found
 342 in this zone. Although there exist abundant relatively smaller craters, the distribution
 343 of the dTB values is not related to the craters distribution. Interestingly, Figure 4(c) shows
 344 that there is a zone with relatively higher FTCs centered at point B (83.3°E, 56.3°N),
 345 and the FTCs largely agree with the highest dTB anomaly at 19.35 GHz, indicating that
 346 strongly correlation between the dTB and the FTCs. Therefore, the high dTB anomaly
 347 should be attributed to the high FTCs.

348 Hiesinger and Head (2003) categorized this region into HU6 unit aged 3.67 Ga in
 349 the western part and HU9 unit aged 3.58 Ga in the eastern part. However, the bound-
 350 aries are not identified by the dTB maps, which indicates the evenly high values in the
 351 two units. Moreover, the FTCs show that the dTB in the middle-western part of the Basin
 352 floor (HU11 unit defined by Hiesinger et al. (2011)) are apparently higher than those in
 353 the place with high dTB anomaly, while the dTB in the former is similar to the latter
 354 at 3.0 GHz and it is much lower than that in the latter at the other three channels. Meng
 355 et al. (2018, 2019, 2020) proposed that the dTB is strongly correlated to the FTCs, and
 356 the regions with higher FTCs have higher dTB values. Thus, the FTCs of the lunar reg-
 357 olith the region with high dTB anomaly should be higher than those in HU11 unit. But
 358 Figure 4 presents a different view about the aforementioned conclusion, where the FTCs
 359 of the lunar regolith the region with high dTB anomaly are lower than those in HU11
 360 unit. There occurs several abnormally high dTB performances besides that in the east-
 361 ern part of the basin floor (Figure 4(c)):

362 The first one is located in the southern part of HU11 unit (Figure 1). The anomaly
 363 is extended from the crater centered at point C (79.6°E, 54.7°N) to the southeast rim
 364 of a crater centered at point D (77.0°E, 56.5°N). Here, the dTB is similar as its vicin-
 365 ity at 3.0, 7.8, and 19.35 GHz, but it is apparently higher than its vicinity at 37 GHz.
 366 The FTC maps (Figure 7(a) and (b)) present the high FTCs in this region, but the dis-
 367 tribution of the high dTB anomaly does not agree with the FTC maps.

368 The second to fourth anomalies are located in the places centered at point E (81.2°E,
 369 54.8°N), point F (84.0°E, 54.4°N), and point G (85.5E, 54.8N), which are clearly not re-
 370 lated to the topography. There exist abundant surface fractures in the crater point H
 371 (80.6°E, 54.5°N) near the site at point E (81.2E, 54.8N). Moreover, a clear depression
 372 occurs in the northeast part of the crater centered at point H (80.6°E, 54.5°N), indicat-
 373 ing the ever-existed strong tectonic activities in this site.

374 The fifth and sixth anomalies are located in the places centered at point I (86.3°E,
 375 52.7°N) and point J (77.5°E, 52.1°N), the southern wall beyond the basin floor. How-
 376 ever, both the FTCs do not support the high dTB anomalies. We mentioned that the
 377 crater density is fairly high in the fifth anomaly. Moreover, a probably rille is just in the
 378 east part. Additionally, there occurs a small patch with relatively smooth surface with
 379 lower topography in the sixth anomaly.

4.3 Correlation analysis of TB distributions

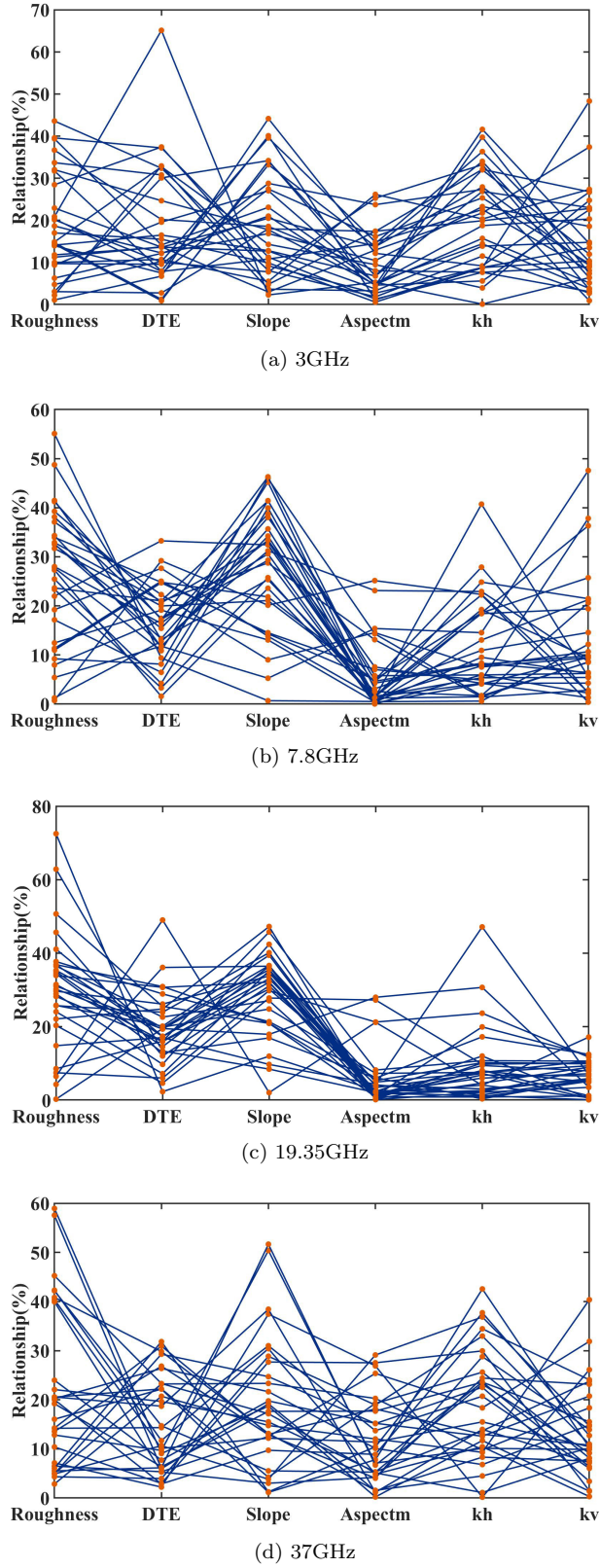


Figure 9: Correlation analysis of dTB values and surface parameters based on BPNN method (Li et al., 2017). Most of the dTB values are related to DTE (Lan et al., 2020) at 3GHz, Slope at 7.8GHz and 19.35GHz, Roughness (Cao et al., 2018) at 37GHz, respectively.

Table 2: Average statistical values of the correlation results based on the BPNN training

Surface parameters	Related percentage (dTB)			
	3GHz	7.8GHz	19.35GHz	37GHz
Roughness	18.31	25.74	29.97	21.41
DTE	18.33	16.36	19.33	15.14
Slope	18.66	27.81	28.74	19.36
Aspectm	9.77	5.61	5.80	11.83
kh	19.95	9.33	20.96	18.87
kv	14.96	12.57	8.81	13.39

381 In this part, the statistical correlations between multichannel dTB distributions
382 and the surface parameters are discussed to interpret what topographic features can be
383 related to the TB variations. In other word, the correlation analysis provides a way to
384 show how TB reflects the topographic features of the studying region.

In general, the correlations between different surface parameters are difficult to show linear relationships. Li et al. (2017) proposed a non-linear approximation called back propagation neural network (BPNN) for analyzing the topographic statistical correlation. The BPNN contains one input layer, one hidden layer, and one output layer for training the selected parameters and obtaining the correlation values (unit: %). The related matrix containing the information of the input surface parameters (roughness, DTE, Slope, Aspectm, kh, kv) are defined as:

$$M_R = \begin{bmatrix} x_{1,1} & x_{1,2} & \dots & x_{1,M} \\ x_{2,1} & x_{2,2} & \dots & x_{2,M} \\ \vdots & \vdots & \vdots & \vdots \\ x_{6,1} & x_{6,2} & \dots & x_{6,M} \end{bmatrix} \quad (12)$$

where M_R denotes the related matrix with the input surface parameters. M denotes the number of the input values contained in the study area. Each row of M_R ($[x_{i,n}|i = 1, 2, \dots, 6, m = 1, 2, \dots, M]$) contains the values of selected surface parameters. Thus, the relationship between dTB and M_R can be expressed as:

$$dTB = w_{ih} \times w_{ho} \times M_R \quad (13)$$

385 Through the BPNN training, the correlation weight matrix (w_{ih} and w_{ho}) can be ob-
386 tained, where w_{ih} denotes the weight matrix between the input layer and the hidden layer,
387 and w_{ho} denotes the weight matrix between the hidden layer and output layer. The cor-
388 relation sequence w is defined as $w_{ih} \times w_{ho}$, where $w = [w_1, w_2, \dots, w_6]$. In this study,
389 the input order of the surface parameters can be seen in Figure 9. Each element in se-
390 quence is related to the values in the related row of M_R . For example, w_1 denotes the
391 correlation value between dTB and topographic roughness.

392 Since the statistical results of correlations are disordered (Figure 9), the averaged
393 related percentage is calculated to indicate the differences of correlations between the
394 multichannel dTBs and surface parameters in Table 2. At 3GHz, dTB values are affected
395 by the subsurface materials (e.g., FTCs in Figure 7). kh indicates highest related per-
396 centage that can agree with this features of dTB variations, because kh reflects the to-
397 pographic variations in the horizontal directions and high FTCs show large clusters on
398 the subsurface (Figure 7). At 7.8GHz, the high-cratered areas and topographic bulges
399 (see HU9 and HU11 in Figure 1), which indicate high topographic vertical variations,
400 show high dTBs (from 11 to 12). Therefore, the highest related percentage of Slope can

401 agree with this result. At 19.35 and 37GHz, dTB reflects the thermal features on lunar
 402 surface, these features influence different types of geological units in the floor. These ge-
 403 ological units are generally complex and irregular (see HU9 and HU11 in Figure 1). These
 404 complex geological units always show high topographic roughness at hectometer- and
 405 kilometer-scales (Rosenburg et al., 2011; Kreslavsky et al., 2013; Cao et al., 2015, 2018)
 406 . Therefore, the highest related percentage can statistically interpret the dTB variations
 407 at these channels.

408 Thus, the multichannel dTB distributions indicate more and more complex topo-
 409 graphic variations following with the frequency increases.

410 5 Conclusion

411 In this paper, we create the dTB maps based on Chang'E-2 microwave radiome-
 412 ter data to improve the understanding of the geological unit divisions and formation pro-
 413 cesses of Mare Humboldtianum. Moreover, the BPNN method provides a way to ana-
 414 lyze the relation between multichannel dTB values and the surface parameters. The main
 415 results are concluded as follows:

- 416 1. The dTB performances in Mare Humboldtianum were strongly affected by the topog-
 417 raphy. Most of the topographic effect were found in the large craters in the basin floor.
 418 The strong correlation results were also be observed by the comparison with FTC maps.
- 419 2. The basaltic units identified previously are not recognized by the dTB maps. The dTB
 420 maps indicated that there should exist two different mare activities in the eastern and
 421 western parts in the basin floor.
- 422 3. Several abnormally high dTB performances were found in the eastern part of the basin
 423 floor. These new founding indicated that most of the dTB anomalies indicated the
 424 strong correlation with the special tectonic features.
- 425 4. The BPNN method was first used to analyze the statistical relations between TB vari-
 426 ations and the surface parameters. Multichannel TB variations reflected different to-
 427 pographic features. At 3GHz, different types of terrains indicated similar dTB dis-
 428 tributions. The geological units with high elevation differences showed strong statisti-
 429 cal correlations with dTB distributions at 7.8GHz, respectively. At 19.35and 37GHz,
 430 the dTB variations in the clusters were complex.

431 Acknowledgments

432 The authors thank Quickmap Team to provide the helpful software for analysis (avail-
 433 able at <https://quickmap.lroc.asu.edu/>), and GMT Team for helpful software (down-
 434 loaded at <https://www.generic-mapping-tools.org/>). The TB data are avialable on-
 435 line (at <http://moon.bao.ac.cn>). The data for roughness calculation and mapped are
 436 download from LOLA PDS Data Node (at <http://imbrium.mit.edu/>). This work was
 437 supported in part by the National Natural Science Foundation of China (No. 42071309),
 438 in part by the Science and Technology Development Fund of Macau under Grant 0052/2020/AFJ,
 439 Grant 0038/2020/A, Grant 0012/2018/A1, and Grant 0069/2018/A2, in part by the Open
 440 Fund of the State Key Laboratory of Remote Sensing Science under Grant OFSLRSS201901,
 441 in part by the Open Project Program of the State Key Laboratory of Virtual Reality
 442 Technology and Systems at Beihang University under Grant VRLAB2019C02, and in
 443 part by the grants from Guangdong Provincial College Innovative Project (No. 2018KQNCX346,
 444 No. 2018KTSCX300, and No. 2019KZDXM060).

445 References

446 Ahmadzadeh, M. R., & Petrou, M. (2001, September). Error statistics for slope and
 447 aspect when derived from interpolated data. *IEEE T. Geosci. Rmote*, 39(9),

- 1823-1833. doi: 10.1109/36.950801
- 448 B. Li and X. Wang and J. Zhang and J. Chen and Z. Ling. (2016, Jun.). Lunar
449 textural analysis based on WAC-derived kilometer-scale roughness and entropy
450 maps. *Planet. Space Sci.*, *125*, 62-71. doi: 10.1016/j.pss.2016.03.004
- 451 Baker, D. M. H., Head, J. W., Neumann, G. A., Smith, D. E., & Zuber, M. T.
452 (2012, March). The transition from complex craters to multi-ring basins on the
453 Moon: Quantitative geometric properties from Lunar Reconnaissance Orbiter
454 Lunar Orbiter Laser Altimeter (LOLA) data. *J. Geophys. Res. Planets*, *117*,
455 E00H16. doi: 10.1029/2011JE004021
- 456 Barker, M. K., Mazarico, E., Neumann, G. A., Zuber, M. T., Haruyama, J., &
457 Smith, D. E. (2016, July). A new lunar digital elevation model from the Lunar
458 Orbiter Laser Altimeter and SELENE Terrain Camera. *Icarus*, *273*, 346-355.
459 doi: 10.1016/j.icarus.2015.07.039
- 460 Booker, J. R., Kovach, R. L., & Lu, L. (1970, November). Mascons and lunar grav-
461 ity. *J. Geophys. Res.*, *75*(32), 6558-6564. doi: 10.1029/JB075i032p06558
- 462 Cai, Y., & Fa, W. (2020). Meter-scale topographic roughness of the moon: The
463 effect of small impact craters. *J. Geophys. Res. Planets*, *125*(e2020JE006429).
464 doi: 10.1029/2020JE006429
- 465 Cao, W., & Cai, Z. (2018, July). Improved multiscale roughness algorithm for lunar
466 surface. *IEEE J. Sel. Topics Appl. Earth Observ. Remote Sens.*, *11*(7), 2336-
467 2345. doi: 10.1109/JSTARS.2018.2822297
- 468 Cao, W., Cai, Z., & Tang, Z. (2015, June). Fractal structure of lunar topography:
469 An interpretation of topographic characteristics. *Geomorphology*, *238*, 112-118.
470 doi: 10.1016/j.geomorph.2015.03.002
- 471 Cao, W., Cai, Z., & Ye, B. (2018, Mar.). Measuring multiresolution surface rough-
472 ness using V-system. *IEEE Trans. Geosci. Remote Sens.*, *56*(3), 1497-1506.
473 doi: 10.1109/TGRS.2017.2764519
- 474 Fa, W., Cai, Y. Z., & Tian, W. (2016, April). Topographic roughness of the north-
475 ern high latitudes of Mercury from MESSENGER Laser Altimeter data. *Geo-*
476 *phys. Res. Lett.*, *43*, 3078-3087. doi: 10.1002/2016GL068120
- 477 Fang, T., & Fa, W. (2014, April). High frequency thermal emission from the lunar
478 surface and near surface temperature of the Moon from Chang'E-2 microwave
479 radiometer. *Icarus*, *232*, 34-53. doi: 10.1016/j.icarus.2013.12.024
- 480 Fassett, C. I., Head, J. W., Kadish, S. J., Mazarico, E., Neumann, G. A., Smith,
481 D. E., & Zuber, M. T. (2012, February). Lunar impact basins: Stratigraphy,
482 sequence and ages from superposed impact crater populations measured from
483 Lunar Orbiter Laser Altimeter (LOLA) data. *J. Geophys. Res. Planets*, *117*,
484 E00H06. doi: 10.1029/2011JE003951
- 485 Feng, J., Siegler, M. A., & Hayne, P. O. (2020, January). New Constraints on Ther-
486 mal and Dielectric Properties of Lunar Regolith from LRO Diviner and CE-2
487 Microwave Radiometer. *J. Geophys. Res-Planet*, *125*(1), e2019JE006130. doi:
488 10.1029/2019JE006130
- 489 Fortezzo, C. M., Spudis, P. D., & Harrel, S. L. (2020, March). Release of the digital
490 unified global geologic map of the Moon. In *Lunar sci. conf. 51st*.
- 491 Freed, A. M., Johnson, B. C., Blair, D. M., Melosh, H. J., Neumann, G. A., Phillips,
492 R. J., ... Zuber, M. T. (2014, September). The formation of lunar mascon
493 basins from impact to contemporary form. *J. Geophys. Res. Planets*, *119*,
494 2378- 2397. doi: 10.1002/2014JE004657
- 495 Head, J. W., Fassett, C. I., Kadish, S. J., Smith, D. E., Zuber, M. T., Neumann,
496 G. A., & Mazarico, E. (2010, September). Global distribution of large lunar
497 craters: Implications for resurfacing and impactor populations. *Science*, *329*,
498 1504. doi: 10.1126/science.1195050
- 499 Hiesinger, H., & Head, J. W. (2003, July). Ages and stratigraphy of mare basalts in
500 Oceanus Procellarum, Mare Nubium, Mare Cognitum, and Mare Insularum. *J.*
501 *Geophys. Res.*, *108*(E7), 5065. doi: 10.1029/2002JE001985
- 502

- 503 Hiesinger, H., Head, J. W., Wolf, U., Jaumann, R., & Neukum, G. (2010, March).
 504 Ages and stratigraphy of lunar mare basalts in mare frigoris and other nearside
 505 maria based on crater size-frequency distribution measurements. *J. Geophys.*
 506 *Res.*, *115*, E03003. doi: 10.1029/2009JE003380
- 507 Hiesinger, H., Head, J. W., Wolf, U., Jaumann, R., & Neukum, G. (2011, March).
 508 Ages and stratigraphy of lunar mare basalts: A synthesis. In (Vol. 477, p. 1-
 509 51). Recent Advances and Current Research Issues in Lunar Stratigraphy. doi:
 510 10.1130/2011.2477(01)
- 511 Hiesinger, H., Jaumann, R., Neukum, G., & Head, J. W. (2000, December). Ages of
 512 mare basalts on the lunar nearside. *J. Geophys. Res.*, *105*(E12), 29239-29275.
 513 doi: 10.1029/2000je001244
- 514 Hiesinger, H., Oberst, J., Jaumann, R., Neukum, G., & Head, J. W. (1996, March).
 515 Observations of Mare Humboldtianum: Topography, ages and multispec-
 516 tral characteristics. In *Lunar sci. conf. 27th* (p. 547-548). Retrieved from
 517 <https://www.lpi.usra.edu/meetings/lpsc1996/pdf/1274.pdf>
- 518 Hu, G., Chan, K., Zheng, Y., & Xu, A. (2018, September). A rock model for
 519 the cold and hot spots in the Chang'E microwave brightness tempera-
 520 ture map. *IEEE T. Geosci. Remote.*, *56*(9), 5471-5480. doi: 10.1109/
 521 TGRS.2018.2817654
- 522 Hu, G., Zheng, Y., Xu, A., & Tang, Z. (2015, December). Microwave bright-
 523 ness temperature of the Moon: The possibility of setting a calibration
 524 source of the lunar surface. *IEEE Geosci. Remote S.*, *13*(2), 182-186. doi:
 525 10.1109/LGRS.2015.2504543
- 526 Kreslavsky, M. A., & Head, J. W. (2000, November). Kilometer-scale roughness of
 527 Mars: Results from MOLA data analysis. *J. Geophys. Res.*, *105*(E11), 26695-
 528 26711. doi: <https://doi.org/10.1029/2000JE001259>
- 529 Kreslavsky, M. A., Head, J. W., Neumann, G. A., Rosenburg, M. A., Aharonson,
 530 O., Smith, D. E., & Zuber, M. T. (2013, September). Lunar topographic
 531 roughness maps from Lunar Orbiter Laser Altimeter (LOLA) data: Scale de-
 532 pendence and correlation with geologic features and units. *Icarus*, *226*(1),
 533 52-66. doi: 10.1016/j.icarus.2013.04.027
- 534 Lan, T., & Cai, Z. (2018, December). Lunar brightness temperature map and TB
 535 distribution model. *IEEE T. Geosci. Remote*, *6*(12), 7310-7323. doi: 10.1109/
 536 TGRS.2018.2850034
- 537 Lan, T., Cai, Z., & Ye, B. (2020, June). Modeling of lunar digital terrain entropy
 538 and terrain entropy distribution model. *IEEE T. Geosci. Remote*, 1-15. doi: 10
 539 .1109/TGRS.2020.2999582
- 540 Li, A., Cai, Z., & Cao, W. (2017, Dec.). Correlation analysis between lunar
 541 surface roughness and other land-surface parameters using BPNN. *IEEE*
 542 *J. Sel. Topics Appl. Earth Observ. Remote Sens.*, *10*(12), 5647-5656. doi:
 543 10.1109/JSTARS.2017.2746899
- 544 Meng, Z., Chen, S., Wang, Y., Wang, T., Cai, Z., Zhang, Y., ... Hu, S. (2020,
 545 February). Reevaluating Mare Moscoviense and its vicinity using Chang'E-2
 546 Microwave Sounder Data. *Remote Sens.*, *12*(535). doi: 10.3390/rs12030535
- 547 Meng, Z., Hu, S., Wang, T., Li, C., Cai, Z., & Ping, J. (2018, September). Passive
 548 microwave probing Mare Basalts in Mare Imbrium using CE-2 CELMS data.
 549 *IEEE J. Sel. Topics Appl. Earth Observ. Remote Sens.*, *11*(9), 3097-3104. doi:
 550 10.1109/JSTARS.2018.2845417
- 551 Meng, Z., Wang, Y., Chen, S., Zheng, Y., Shi, J., Wang, T., ... Hou, L. (2019,
 552 May). MTE features of Apollo Basin and its significance in understanding the
 553 SPA Basin. *IEEE J. Sel. Topics Appl. Earth Observ. Remote Sens.*, *12*(7),
 554 2575-2583. doi: 10.1109/JSTARS.2019.2916061
- 555 Moriarty, D. P., & Pieters, C. M. (2016, January). Complexities in pyroxene compo-
 556 sitions derived from absorption band centers: Examples from Apollo samples,
 557 HED meteorites, synthetic pure pyroxenes, and remote sensing data. *Meteorit.*

- 558 *Planet. Sci.*, 51(2), 207-234. doi: 10.1111/maps.12588
- 559 Oberst, J., Wählisch, M., Zhang, W., Roatsch, T., Cook, A. C., & Jaumann, R.
560 (1996, March). New data on lunar topography derived from Galileo and
561 Clementine stereo images. In *Lunar sci. conf. 27th* (p. 973-974). Retrieved
562 from <https://www.lpi.usra.edu/meetings/lpsc1996/pdf/1487.pdf>
- 563 Olaya, V. (2009). Basic land-surface parameters. In T. Hengl & H. I. Reuter (Eds.),
564 *Geomorphometry: Concepts, Software, Applications* (Vol. 33, p. 141-169). Am-
565 sterdam, The Netherlands: Elsevier.
- 566 Rosenburg, M. A., Aharonson, O., Head, J. W., Kreslavsky, M. A., Mazarico, E.,
567 Neumann, G. A., ... Zuber, M. T. (2011, Feb.). Global surface slopes and
568 roughness of the Moon from the Lunar Orbiter Laser Altimeter. *J. Geophys.*
569 *Res.*, 116(E02001). doi: 10.1029/2010JE003716
- 570 Shepard, M. K., Campbell, B. A., Bulmer, M. H., Farr, T. G., Gaddis, L. R., &
571 Plaut, J. J. (2001, Dec.). The roughness of natural terrain: A planetary and
572 remote sensing perspective. *J. Geophys. Res.*, 106(E12), 32777-32795.
- 573 Smith, D. E., Zuber, M. T., Jackson, G. B., Cavanaugh, J. F., Neumann, G. A.,
574 Riris, H., ... Zagwodzki, T. W. (2010, May). The Lunar Orbiter Laser Al-
575 timeter Investigation on the Lunar Reconnaissance Orbiter Mission. *Space Sci.*
576 *Rev.*, 150, 209-241. doi: 10.1007/s11214-009-9512-y
- 577 Song, R., Ma, H., & Qi, D. (2007, Sep.). The complete orthogonal V-system and its
578 applications. *Commun. Pure Appl. Anal.*, 6(3), 853-871. doi: 10.3934/cpaa
579 .2007.6.853
- 580 Susorney, H. C. M., Barnouin, O. S., Ernst, C. M., & Byrne, P. K. (2017, June).
581 The surface roughness of Mercury from the Mercury Laser Altimeter: Investi-
582 gating the effects of volcanism, tectonism, and impact cratering. *J. Geophys.*
583 *Res. Planets*, 122, 1372-1390. doi: 10.1002/2016JE005228
- 584 Susorney, H. C. M., Barnouin, O. S., Ernst, C. M., & Stickle, A. M. (2018, Jun.).
585 The surface roughness of large craters on Mercury. *J. Geophys. Res. Planets*,
586 123, 1581-1596. doi: 10.1029/2017JE005462
- 587 Susorney, H. C. M., Johnson, C. L., Barnouin, O. S., Daly, M. G., Seabrook, J. A.,
588 Bierhaus, E. B., & Lauretta, D. S. (2019, January). The global surface rough-
589 ness of 25143 itokawa. *Icarus*, 325, 141-152. doi: 10.1016/j.icarus.2019.01.021
- 590 Zheng, Y., Chan, K., Tsang, K., Zhu, Y., Hu, G., Blewett, D. T., & Neish, C. (2019,
591 February). Analysis of Chang'E-2 brightness temperature data and production
592 of high spatial resolution microwave maps of the Moon. *Icarus*, 319, 627-644.
593 doi: 10.1016/j.icarus.2018.09.036
- 594 Zheng, Y., Tsang, K., Chan, K., Zou, Y., Zhang, F., & Ouyang, Z. (2012, May).
595 First microwave map of the Moon with Chang'E-1 data: the role of local time
596 in global imaging. *Icarus*, 219, 194-210. doi: 10.1016/j.icarus.2012.02.017
- 597 Zhu, Y., Zheng, Y., Fang, S., Zou, Y., & Pearson, S. (2019, January). Analysis of
598 the brightness temperature features of the lunar surface using 37 GHz channel
599 data from the Chang'E-2 microwave radiometer. *Adv. Space Res.*, 63, 750-765.
600 doi: 10.1016/j.asr.2018.10.014